Symmetry-Broken Au–Cu Heterostructures and their Tandem Catalysis Process in Electrochemical CO$_2$ Reduction

Henglei Jia, Yuanyuan Yang, Tsz Him Chow, Han Zhang, Xiyue Liu, Jianfang Wang,* and Chun-yang Zhang*

Symmetry-breaking synthesis of colloidal nanocrystals with desired structures and properties has aroused widespread interest in various fields, but the lack of robust synthetic protocols and the complex growth kinetics limit their practical applications. Herein, a general strategy is developed to synthesize the Au–Cu Janus nanocrystals (JNCs) through the site-selective growth of Cu nanodomains on Au nanocrystals, which is directed by the substantial lattice mismatch between them, with the assistance of judicious manipulation of the growth kinetics. This strategy can work on Au nanocrystals with different architectures for the achievement of diverse asymmetric Au–Cu hybrid nanostructures. Of particular note, the obtained Au nanobipyramids (Au NBPs)-based JNCs facilitate the conversion of CO$_2$ to C$_2$ hydrocarbon production during electrocatalysis, with the Faradaic efficiency and maximum partial current density being 4.1-fold and 6.4-fold higher than those of their monometallic Cu counterparts, respectively. The excellent electrocatalytic performances benefit from the special design of the Au–Cu Janus architectures and their tandem catalysis mechanism as well as the high-index facets on Au nanocrystals. This research provides a new approach to synthesize various hybrid Janus nanostructures, facilitating the study of structure-function relationship in the catalytic process and the rational design of efficient heterogeneous electrocatalysts.

1. Introduction

The electrochemical conversion of greenhouse gas CO$_2$ into the value-added fuels and feedstocks represents a green avenue to address the energy demands and climate change issues.[1,2] One of the greatest challenges for this conversion is to develop catalysts with the capability of reducing CO$_2$ into more valuable products. Among various metal electro-catalysts, Cu has attracted great interest as the catalyst for electrocatalytic CO$_2$ reduction reaction (CO$_2$RR) due to its unique capability of converting CO$_2$ into a wide spectrum of useful products, such as C$_1$ (CO, CH$_4$, formate) and C$_2$ (C$_2$H$_4$, C$_2$H$_6$) products, but poor selectivity is a major drawback.[3–6] From the fundamental perspective, poor selectivity originates from the moderate binding energy of most reaction intermediates.[7] In comparison with C$_1$ products, C$_2$ products are more appealing because of their higher energy density and larger economic value. Considerable efforts have been devoted to the unraveling of various factors that impact the C$_2$ product activity and selectivity,[8–10] including the manipulation of catalyst morphology,[11–15] controlling of oxide state,[16–20] engineering of crystal facet,[21,22] and surface modification.[23,24] However, it has remained a great challenge for monometallic Cu catalysts to efficiently convert CO$_2$ into C$_2$ products.

Recent advances have brought Cu-based bimetallic catalysts to the forefront for the improvement of C$_2$ selectivity during CO$_2$RR. The associated variations in composition, electronic structure, and spatial elemental distribution of bimetallic catalysts can alter the intermediate binding energetics.[7,25–28] Au nanocrystals have aroused extraordinary interest in the fields of photocatalysis,[29,30] optics,[31] and biomedical technologies[32,33] due to their well-controlled morphologies and unique plasmonic properties, but their applications in CO$_2$RR are still at their infancy. Au nanocrystals have recently shown great promise as catalysts for efficient CO$_2$ reduction to CO with good selectivity.[34–37] Since the adsorbed CO is critical for C—C bond coupling and the subsequent formation of C$_2$ products,[38] the integration of Au nanocrystals with Cu catalysts is expected to improve the C$_2$ selectivity through a tandem catalysis mechanism,[39–41] where CO$_2$ is reduced to CO on the Au nanocrystal and subsequently reduced on the neighboring Cu component. However, what really matters for the tandem catalysis process is the geometric arrangement of Au and Cu in the bimetallic catalyst.[26,27,42] For example, the phase-separated bimetallic nanostructures facilitate the C$_2$ production compared with the alloy type.[42] Inspired from the ancient two-faced Roman god Janus,

Prof. H. L. Jia, Y. Y. Yang, X. Y. Liu, Prof. C.-Y. Zhang
College of Chemistry
Chemical Engineering and Materials Science
Collaborative Innovation Center of Functionalized Probes for Chemical
Imaging in Universities of Shandong
Key Laboratory of Molecular and Nano Probes
Ministry of Education
Shandong Provincial Key Laboratory of Clean Production
of Fine Chemicals, Shandong Normal University
Jinan 250014, China
E-mail: cyzhang@sdnu.edu.cn
Dr. T. H. Chow, Dr. H. Zhang, Prof. J. F. Wang
Department of Physics
The Chinese University of Hong Kong
Shatin, Hong Kong SAR, China
E-mail: jfwang@phy.cuhk.edu.hk

the Janus nanostructures comprising two or more spatially separated components with dissimilar physical and chemical functionalities have triggered extraordinary interests in various fields due to their intricate properties and potential applications.[43] Unlike the centrosymmetric core@shell nanostructures with the exposure of the only outermost shell surface, asymmetric Janus nanostructures possess two or more different surfaces with at least one sharing heterointerface. These diverse surfaces in Janus structures can participate and play different roles in the catalytic process, endowing them with desired catalytic features and even synergistic effects. Because of their unique architecture, the synthesis of Janus nanostructures is required to employ unconventional synthesis approaches like symmetry-breaking synthesis (e.g., surface-protection growth, kinetically controlled manipulation, and seed-mediated growth).[44–48] However, the lack of a universal synthetic strategy to obtain the Au–Cu Janus nanocrystals (JNCs) strongly restricts their further applications in CO_2RR. Therefore, the development of spatially separated Au–Cu JNC catalysts for the sustainable production of C_2 products is highly desirable.

Herein, we develop a facile and general approach for the synthesis of Au–Cu JNCs through a seed-mediated growth method by taking advantage of a relatively large lattice mismatch ($\approx$11.4%) between them[49] in combination with the judicious manipulation of the surfactant concentration. The penta-twinned Au nanobipyramids (Au NBPs) are used as the seeds for the direct overgrowth of Cu nanodomains. Owing to the large lattice mismatch, Cu selectively overgrows on the side surface of the Au NBPs through controlling the growth kinetics, leading to the formation of spatially separated Au–Cu heterostructures. This site-selective overgrowth protocol can be simply extended to various Au cores, from 0D, 1D, to 2D Au nanocrystals, suggesting the generality of the proposed method. To the best of our knowledge, our research demonstrates for the first time the development of a general method for the preparation of Au–Cu Janus heterostructures. In addition, the tandem catalysis process resulting from the unique spatially separated architecture and the high-index facets of Au NBPs endows the Au–Cu JNCs with much higher C_2 activity and good selectivity, with the Faradaic efficiency (FE) and the maximum partial current density being 4.1-fold and 6.4-fold compared with those of the monometallic Cu counterparts.

2. Results and Discussion

Scheme 1a illustrates the site-selective growth process of a Cu nanodomain on the side surface of a Au NBP to produce the Au NBP–side Cu JNCs (Au NBP–Cu JNCs). Each Au NBP featuring a fivefold rotational symmetry structure and consisting of two base-stacked pentagonal pyramids[50] is utilized as the seed. The crystalline structure of a Au NBP is depicted in Figure S1, Supporting Information, with each NBP being encapsulated with 10 facets.[51,52] The side facets are stepped periodically along the length direction to form the high-index {116} facets.[50,51] Cu atoms are expected to initially nucleate on one high-index {116} facet, because the Au atoms at the steps are generally coordinately unsaturated and are more active for the nucleation of Cu (Scheme 1a, the first step). Due to the considerable lattice
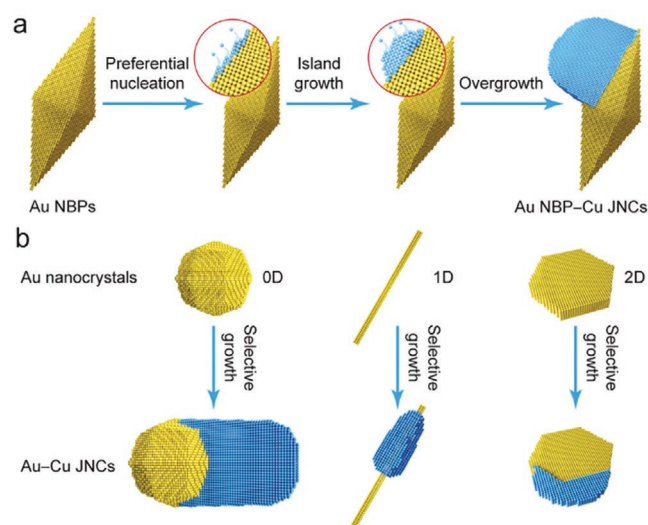
Scheme 1. a) Schematic illustration for the selective growth process of a Au NBP–Cu hybrid nanostructure. b) Schematic showing the generality of the site-selective growth strategy for Au nanocrystals with different architectures.

mismatch ($\approx$11.4%) between Au and Cu,[49] the growth of Cu on the Au NBPs prefers to adopt the classic Volmer–Weber model through a 3D island growth (Scheme 1a, the second step).[49,53] Further deposition of Cu atoms will mainly take place at the original Cu surface in order to minimize new interfacial free energy resulting from the Au–Cu nanointerface (Scheme 1a, the third step). Consequently, the Au NBP–Cu hybrid nanostructures featured with Au and Cu nanodomains and a sharing interface are obtained. Notably, the site-selective overgrowth protocol can work on Au nanocrystals with different architectures, leading to the formation of diverse asymmetric Au–Cu hybrid nanostructures (Scheme 1b).

The penta-twinned Au NBPs are obtained through the seed-mediated growth method in combination with a depletion force-induced purification process.[54,55] The average length and middle diameter are 103.4 ± 2.9 and 34.6 ± 1.9 nm, respectively (**Figure 1**a). The representative low-magnification transmission electron microscopy (TEM) image of the Au NBP–Cu JNCs is shown in Figure 1b with the Cu nanodomains (47.3 ± 2.9 nm) on the side surface of the Au NBPs. To uncover such a heterostructure feature, high-angle annular dark-field scanning transmission electron microscopy (HAADF-STEM) imaging and elemental mapping were conducted (Figure 1c). The results clearly reveal the presence of spatially separated Au and Cu nanodomains with a sharp interface contacting with each other. After the growth of Cu nanodomain, the plasmon resonance peak of the Au NBPs red-shifts, accompanied by a broad peak, which is caused by the overgrowth of Cu (Figure S2a, Supporting Information). A remarkable increase in the extinction below 600 nm is observed for the Au NBP–Cu JNCs, suggesting the presence of excess hexadecylamine (HDA)–Cu complex in the solution.[56] The successful overgrowth of Cu on the Au NBPs is confirmed by the color change from reddish-brown to yellow-brown (Figure S2a, Supporting Information). Notably, the low-magnification TEM image (Figure S3, Supporting Information)
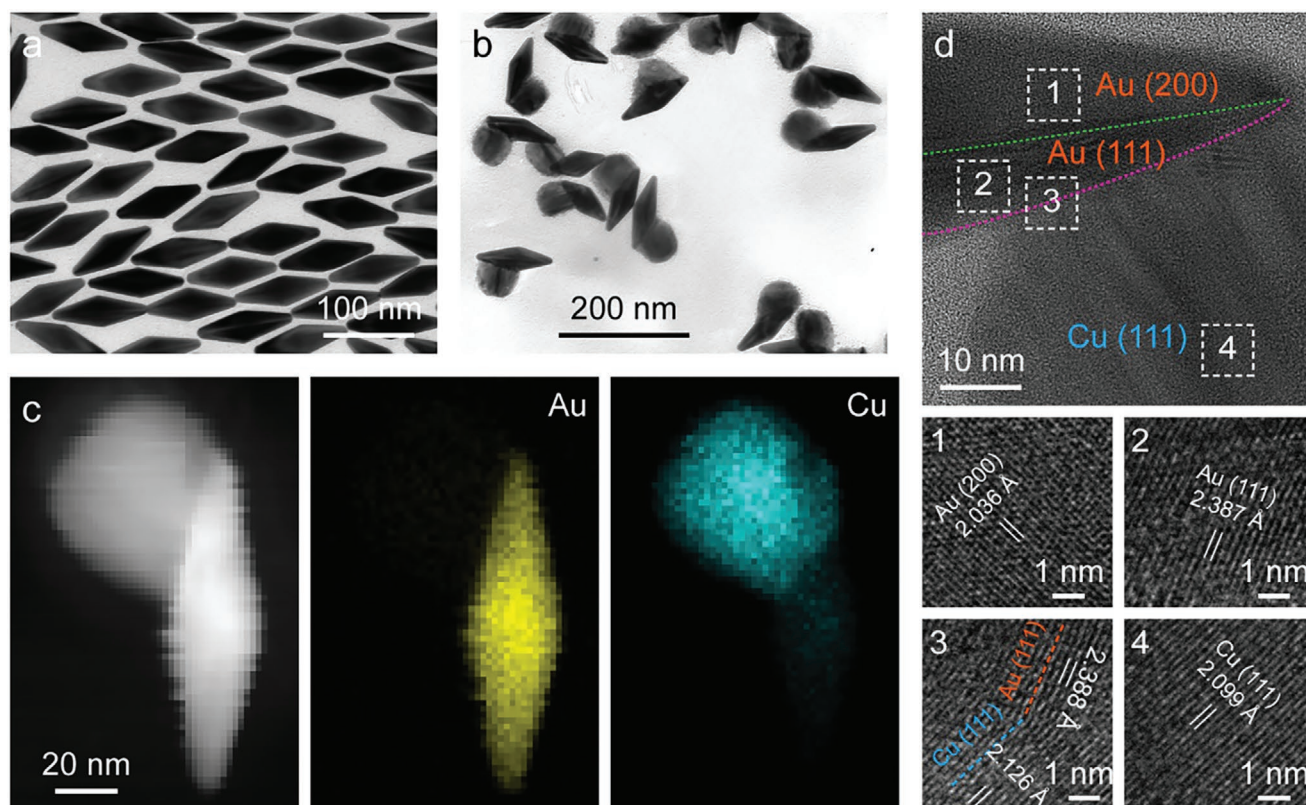
Figure 1. Au NBP–Cu JNCs. a,b) TEM images of the as-synthesized Au NBPs (a) and Au NBP–Cu JNCs (b). c) HAADF-STEM image (left) and the corresponding elemental maps of Au (middle) and Cu (right) of a representative Au NBP–Cu heterostructure. d) Aberration-corrected HRTEM images at the Au–Cu interface of single Au NBP–Cu JNC. Four typical regions are marked by dashed white boxes (1–4) and the corresponding enlarged images identify the facets of Au and Cu.

reveals a high yield (≈96%) of the Au NBP–Cu JNCs. To gain a deep insight into the overgrowth behavior of the Cu nanodomain on the Au NBPs, we took the aberration-corrected high-resolution TEM (HRTEM) images of the Au–Cu interface (Figure 1d). As expected, the Cu nanodomain is mainly grown on the Au {111} facet, which confirms the proposed growth mechanism. In addition, the lattice fringes of the Cu {111} facets at the Au–Cu interface (Figure 1d 3) are slightly wider than the theoretical value (2.088 Å) due to the misfit dislocation at the interface as a result of a large lattice mismatch. The lattice mismatch value calculated from the lattice fringes at the Au–Cu interface is 11.0%, consistent with the reported value of 11.4%.[49] Moreover, the lattice fringes turn gradually close to the theoretical value when they are away from the interface, indicating the release of lattice strain. Above all, the aberration-corrected HRTEM results reveal the growth behavior of Cu nanodomain on the Au NBP.

To examine the crystalline nature and chemical composition of the Au NBP–Cu JNCs, we measured X-ray diffraction (XRD) and X-ray photoelectron spectra (XPS). The XRD spectrum (Figure S4, Supporting Information) shows only two distinct sets of diffraction patterns, indicating the presence of pure metallic Au and Cu phases, consistent with the observation from the high-resolution XPS spectra (Figure S5, Supporting Information). The high-resolution Cu 2p XPS spectrum exhibits two peaks, which can be assigned to the Cu $2p_{3/2}$

(932.9 eV) and Cu $2p_{1/2}$ (952.6 eV) peaks of pure metallic Cu, respectively. The absence of any satellite peaks suggests that the dominant form of Cu in the Au NBP–Cu JNCs is the pure metallic Cu.[56] A wide O 1s peak centered at 531.3 eV originates from either the chemisorbed water or the inevitable occurrence of oxidation upon exposure to air.[25]

Notably, the synthetic protocol works for different pre-grown Au nanocrystals from 0D to 2D, enabling the generation of diverse asymmetric Au–Cu nanostructures. Three typical Au nanocrystals including 0D Au nanospheres (Au NSs), 1D long Au nanorods (Au NRs), and 2D hexagonal Au nanoplates (Au NPLs) were prepared as the seeds to direct the growth of Cu domains (**Figure 2**a–c). The average diameter of the Au NSs, the average length/diameter of the long Au NRs, and the average lateral size of the Au NPLs (which is the perpendicular distance between two parallel edges) are 49.6 ± 3.2, 709.5 ± 38.3 / 25.8 ± 2.4, and 153.2 ± 5.1 nm, respectively. The obtained asymmetric Au–Cu nanostructures are displayed in Figure 2d–f. Obviously, the Au NS–Cu hybrid nanostructures (Au NS–Cu JNCs) are composed of two segregated nanodomains and a shared interface (Figure 2d). Two segregated domains consisting of Au and Cu are verified by the elemental mapping (Figure 2g). The presence of pure metallic Au and Cu phases in the Au NS–Cu JNCs is further verified by HRTEM and XRD (Figure S6, Supporting Information). Analogously, the lattice fringes of the Cu {111} facets at the
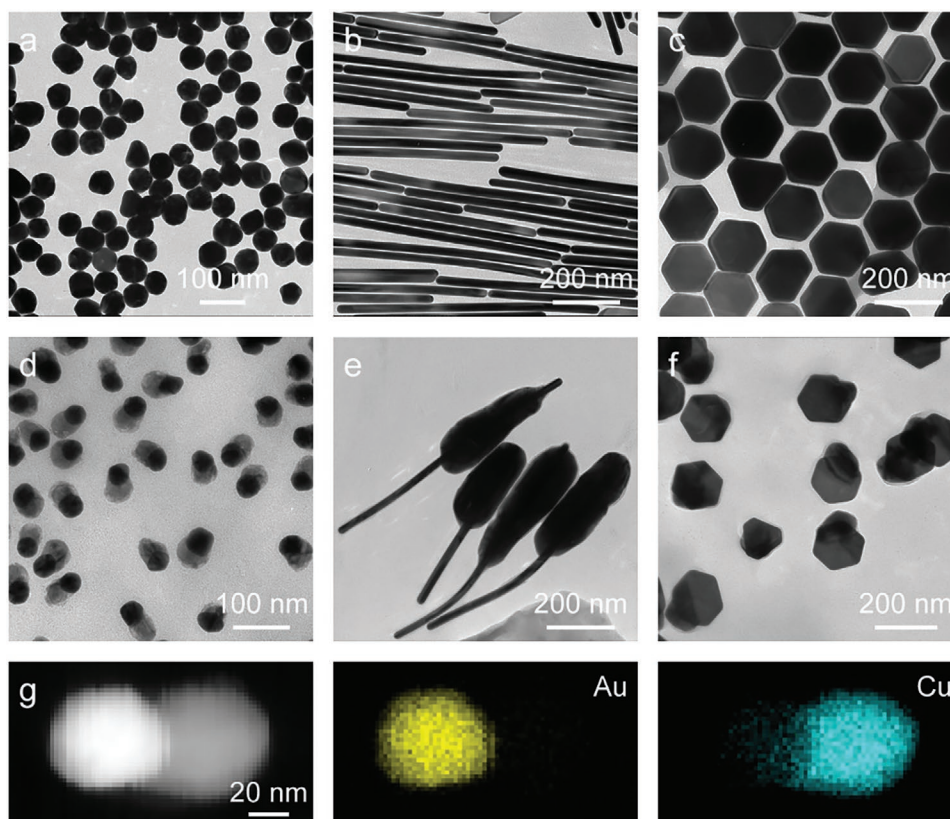
Figure 2. Growth of Cu nanodomains on Au nanocrystals with different morphologies from 0D to 2D. a–c) TEM images of 0D Au NSs (a), 1D long Au NRs (b), and 2D hexagonal Au NPLs (c). d–f) TEM images of the corresponding asymmetric Au–Cu nanostructures. g) HAADF-STEM image (left) and the corresponding elemental maps of Au (middle) and Cu (right) of a representative Au NS–Cu heterostructure.

Au–Cu interface (2.119 Å, Figure S6b, Supporting Information) are also slightly wider than the theoretical value (2.088 Å), but they are smaller than those of the Au NBP–Cu JNCs (2.126 Å, Figure 1d 3). This result suggests that the high-index facets of Au NBPs can cause larger misfit dislocation than that of the low-index facets on Au NSs. Notably, the number yield of the Au NS–Cu JNCs is nearly 100% (Figure S7, Supporting Information), suggesting the good universality of the proposed synthesis strategy. In addition, Cu shell is selectively formed on one end of the long Au NRs with a long tail exposure as a result of the large lattice mismatch (Figure 2e). When the Au NPLs are used as the seeds, Cu nanodomain deposition occurs preferentially on one corner of the hexagonal plates (Figure 2f), because the Au atoms at the corner sites are more undercoordinated and consequently more active in the Cu deposition process.[57] Our above results clearly demonstrate the development of a universal approach for the preparation of Au–Cu JNCs.

We further performed a series of control experiments to investigate the growth behavior. The surfactant concentration plays an important role in the site-selective growth of a second material on Au nanocrystals.[29] We first investigated the effect of cetyltrimethylammonium bromide (CTAB) concentration upon the overgrowth behavior of Cu (Figure S8, Supporting Information). Appropriate low-concentration CTAB (10–200 µM) is required to obtain a high yield of the Au NBP–Cu JNCs (Figure S8a–c, Supporting Information), but extremely low-concentration CTAB may induce the aggregation

of the Au NBPs. When the CTAB concentration is increased to 400 µM, long Cu NRs tend to grow at one end of the Au NBPs (Figure S8d, Supporting Information). Further increase of CTAB concentration (>500 µM) will induce the self-nucleation of Cu nanoparticles (Figure S8e,f, Supporting Information). The nonuniform distribution of the CTAB bilayer is essential to the site-selective growth behavior. At a low CTAB concentration, the CTAB bilayers at the edges of the Au NBPs are packed less compactly than those on the side facets due to the larger curvature (Figure S1, Supporting Information),[29] facilitating the preferential nucleation of Cu at one edge and the subsequent overgrowth of a Cu nanodomain for the covering of adjacent facets. In addition, the high-energy sites at the edges favor preferential Cu deposition. When the CTAB concentration is large enough, all the surfaces of the Au NBPs are densely covered by the surfactant molecules, which hinders the deposition of Cu atoms. Notably, the HDA concentration plays an important role (Figure S9, Supporting Information). HDA is an effective capping agent for Cu nanocrystals due to its amino group-induced strong coordination effect toward Cu (II) ions.[58,59] Appropriate low-concentration Cu (II) ions (≈5 mM) is indispensable for the site-selective growth of Cu on the Au nanocrystals. Since HDA can act as the capping agent for both Cu and Au,[60,61] the adsorption of HDA on the surface of Au nanocrystals can occur at high concentration (10 mM), which may reduce the nonuniform distribution of surfactant molecules and the number yield of the Au NBP–Cu JNCs (Figure S9e, Supporting Information).

**ADVANCED
SCIENCE NEWS**

www.advancedsciencenews.com

**ADVANCED
FUNCTIONAL
MATERIALS**

www.afm-journal.de

On the contrary, low-concentration HDA is inadequate for the adsorption and stabilization of the formed Cu nanodomain on the Au nanocrystal (Figure S9a, Supporting Information). Thus, appropriate-concentration HDA facilitates its binding to the Cu nanodomain and meanwhile does not disturb the distribution of surfactant CTAB on the surface of Au nanocrystals. In addition, the length of the alkyl chain (Figure S10, Supporting Information), the type of precursor (Figure S11, Supporting Information), and the amount of precursor ($CuCl_2$) (Figure S12, Supporting Information) affect the morphology of the Au–Cu hybrid nanostructure as well. In general, the site-selective growth behavior of Cu on the Au NBPs is mainly determined by the concentrations of surfactants and the choice of Cu precursor.

The Cu-based nanomaterials offer exciting opportunities for producing high-value hydrocarbons from CO_2RR.[2,62] The well-defined spatially separated Au–Cu hybrid nanostructure allows for the investigation of the structure-dependent catalytic performances. Two types of Au–Cu JNCs (i.e., the Au NBP–Cu JNCs and the Au NS–Cu JNCs) with high number yields were selected as the catalysts. For comparison, Au NBPs (Figure 1a), Cu nanospheres (Cu NSs) (Figure S13a, Supporting Information), Au NBP@Cu core@shell nanostructures (Figure S13b, Supporting Information), and the mixture of Au NBPs with Cu NSs were prepared as the catalysts. It should be noted that the residual surfactant molecules in these catalysts were not completely removed to stabilize the morphology, which may block the active sites and reduce the activity of catalysts. In addition, the remaining surfactants in these catalysts may influence the CO_2 absorption and subsequently alter the product selectivity. A recent study demonstrated that surfactants in Au catalysts can induce a decrease of mass activity but a negligible change in product selectivity during CO_2RR.[63] In order to investigate the effect of morphology and to maintain the stability of catalysts, the surfactant removal step was not carried out, because the reaction environment and surfactant molecules used for the preparation of Au–Cu JNCs are similar. In addition, the product selectivity is both voltage- and facet-dependent.[64] XRD results have confirmed that the crystalline nature of the Au NS–Cu JNCs (Figure S6, Supporting Information) and the Au NBP–Cu JNCs (Figure S4, Supporting Information) are all same under the similar reaction conditions. For the study of structure-dependent catalytic activity and selectivity, the possible facet effect during CO_2RR is not taken into account. The FE and the current density were used to characterize the electrocatalytic performance.[65] To accurately obtain the FE data, each electrode allows quantitative 5 Coulombs of charges to pass through the catalyst using chronoamperometry (Figure S14, Supporting Information).[17] All electrochemical measurements were performed in a CO_2-saturated 0.1 M $KHCO_3$ aqueous solution with a gastight two-compartment cell, and the products were detected with off-line gas chromatography in combination with ion chromatography. The catalyst-modified flat glassy carbon electrode was employed as the working electrode and was activated prior to each test.

Figure 3 shows the FE results of the major gas products obtained by using six types of catalysts. H_2 is the by-product of CO_2RR and is produced through the electrochemical reduction of water. As shown in Figure 3a, CO is the only CO_2RR product of Au NBP catalyst with a maximal FE of 27.8% at −1.29 V (vs reversible hydrogen electrode (RHE)). Three types of gas products including CO, CH_4, and C_2H_4 are detected in the presence of Cu NS catalyst (Figure 3b). The FE of CH_4 increases linearly when the potential becomes more negative, with CH_4 becoming the dominant product when the potential is more negative than −1.1 V. C_2H_4 is the main C_2 product in the presence of Cu NS catalyst, with an optimal FE of 11.3% at −1.06 V. Similar results are obtained in the presence of the catalyst mixture (Figure 3c). The FE values of C_1 products (i.e., CO and CH_4) increase slightly in the presence of the mixture of Au NBPs and Cu NSs, but there is no significant change in the C_2H_4 selectivity, suggesting the absence of a synergistic effect. The core@shell nanostructures exhibit worse performance than either the Cu NS or the catalyst mixture (Figure 3d) due to the complete blocking of active sites of the Au NBPs. Notably, the CO_2 reduction can only take place on the surface of the Cu shell in the core@shell nanostructures, similar to the Cu NS catalyst, and the larger Cu nanocrystals favor the reduction of water to H_2 rather than CO_2RR.[66] Consequently, the core@shell catalyst with a larger Cu shell (length/diameter is 116.9 ± 10.1 nm / 98.7 ± 9.5 nm) exhibits higher selectivity toward H_2 evolution than the smaller Cu NS (36.2 ± 2.6 nm) and the catalyst mixture. Impressively, the two spatially separated Au–Cu JNCs exhibit much higher C_2 selectivity than the other catalysts (Figure 3e,f). The optimal FE value of C_2H_4 is 22.8% for the Au NS–Cu JNCs and 41.5% for the Au NBP–Cu JNCs. Notably, a new C_2 product (i.e., C_2H_6) produced through 14e reduction[2,67] is obtained for both Au–Cu JNCs, with maximum FE being 5.1% for the Au NBP–Cu JNCs. In addition, the main liquid products obtained by using these six catalysts are all formate, with most of the FEs being smaller than 5% (Figure S15, Supporting Information). Both the Au NS–Cu JNCs and Au NBP–Cu JNCs exhibit better activities toward the liquid product, with the formate FE being 2.1-fold and 2.4-fold compared with that of the Cu NSs, respectively.

To trace the carbon source of the products, control experiments were performed in an Ar-saturated 0.1 M $KHCO_3$ aqueous solution with the Au NBP–Cu JNCs as the catalyst (Figure S16, Supporting Information). H_2 is the only product at different potentials and the obtained FE values are all close to 100%, suggesting that the carbon source of the products is the reduction of CO_2. To investigate the stability of the Au NBP–Cu JNCs, TEM imaging and XRD were obtained after the typical electrocatalytic process. No morphological and structural changes are observed, indicating the excellent stability of the hybrid nanostructures (Figure S17a,b, Supporting Information). In addition, the Au NBP–Cu JNCs retain their catalytic activity at −0.981 V for 10 h (Figure S17c, Supporting Information), suggesting good electrocatalytic stability of the Au NBP–Cu JNCs.

Since C_2 products possess higher energy densities with wider applications than C_1 compounds, their selectivity toward total C_2 products (C_2H_4 + C_2H_6) was further investigated (**Figure 4**). The Au NBPs exhibit no activity toward the C_2 products, while the C_2 FE values of the other catalysts display a volcano-shaped dependence upon the potential (Figure 4a). The optimal FE values of these catalysts are selected and plotted in Figure 4b for comparison. The highest C_2 product FEs of the Au NS–Cu JNCs and Au NBP–Cu JNCs are 25.2 and 46.4%, which are
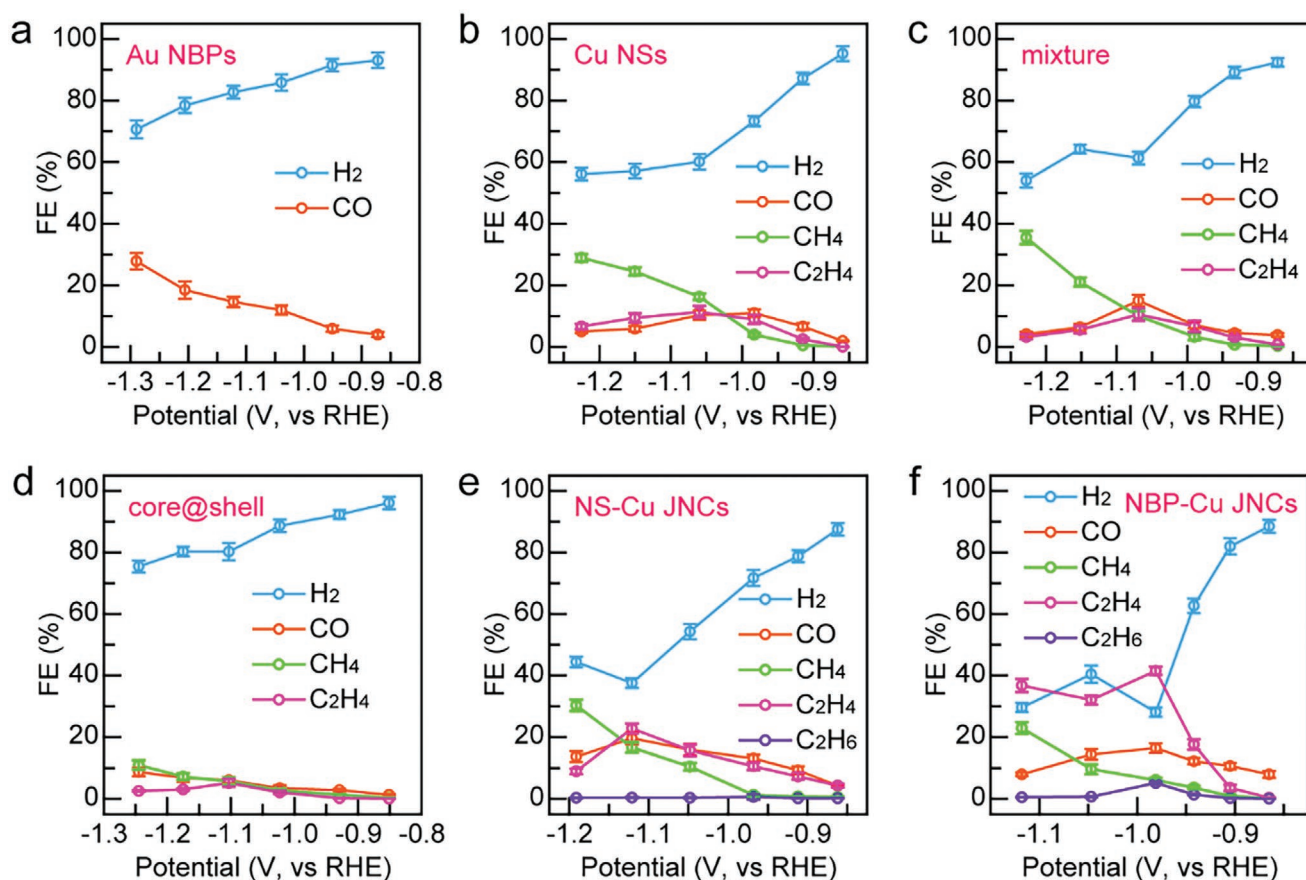
**ADVANCED
SCIENCE NEWS**
www.advancedsciencenews.com

**ADVANCED
FUNCTIONAL
MATERIALS**
www.afm-journal.de

Figure 3. Electrochemical CO_2 reduction performances. The FEs of the major gaseous products obtained by using a) Au NBP, b) Cu NS, c) Au NBP + Cu NS mixture, d) Au NBP@Cu core@shell, e) Au NS–Cu JNC, and f) Au NBP–Cu JNC catalysts, respectively.

2.2-fold and 4.1-fold compared with that of the Cu NS counterpart, respectively, suggesting the synergistic effect of Au and Cu in the hybrid nanostructure. The optimal C_2 FE value of the Au NBP–Cu JNCs is comparable or even superior to the reported Cu-base bimetallic electrocatalysts (Table S1, Supporting Information). In addition, the catalyst mixture exhibits a similar C_2 performance as the Cu NSs, suggesting that the formation of a directly contacted interface between Au and Cu is the decisive factor for the improvement of C_2 selectivity. The catalytic activities were further investigated by measuring the current densities at different potentials. As shown in Figure 4c, both Au–Cu JNCs exhibit higher total activities than the Cu NS counterparts. It should be noted that the total current density is contributed by the reduction of water to H_2 and the reduction of CO_2 to both C_1 and C_2 products. To pinpoint the proportion of the C_2 activity, we compared the partial current densities for C_2 production obtained by using different catalysts (Figure 4d). Impressively, the Au NBP–Cu JNCs induce significant improvement of C_2 activity compared with the Cu NS counterparts, with maximum partial current density on the Au NBP–Cu JNCs (at −1.118 V) being 6.4-fold higher than that of the Cu NS sample (at −1.06 V). A decrease peak in the partial current density of the Au NBP–Cu JNCs (at −1.05 V) (Figure 4d) originates from the decrease of both C_2H_4 and C_2H_6 FE values at this potential. Therefore, the Au NBP–Cu heterostructure featured with the

spatially separated Au and Cu nanodomains and the unique Au NBP structural property facilitates the conversion of CO_2 to C_2 products.

The C−C coupling is crucial to the generation of the C_2 products in CO_2RR, and it is highly sensitive to the structure and composition of catalyst. Cu is the unique metal catalyst with the capability of producing high-value hydrocarbons during CO_2RR, but it suffers from poor selectivity due to its moderate binding energies with most reaction intermediates.[2] The low O and H affinities endow Au with a weak binding energy for the CO intermediate, which makes CO become the major product.[7] A tandem catalysis process is feasible as an alternative mechanism for high C_2 activity and selectivity of the Au–Cu heterostructures.[39] In this tandem catalysis process, CO is generated on the Au catalyst through the reduction of CO_2, and subsequently migrates to the active sites of nearby Cu for further CO dimerization, which is the rate-determining step in the C_2 pathway. However, this tandem catalysis process relies heavily on the spatial arrangement of Au and Cu components in the nanostructure. In the catalyst mixture, the tandem catalysis process is very weak due to the large distance between them and the poor solubility of CO, resulting in the separate catalysis by Au and Cu independently (**Figure 5**a). In the core@ shell nanostructure, the Au component is buried inside the Cu shell, which hinders the access of Au to reactant CO_2 molecules
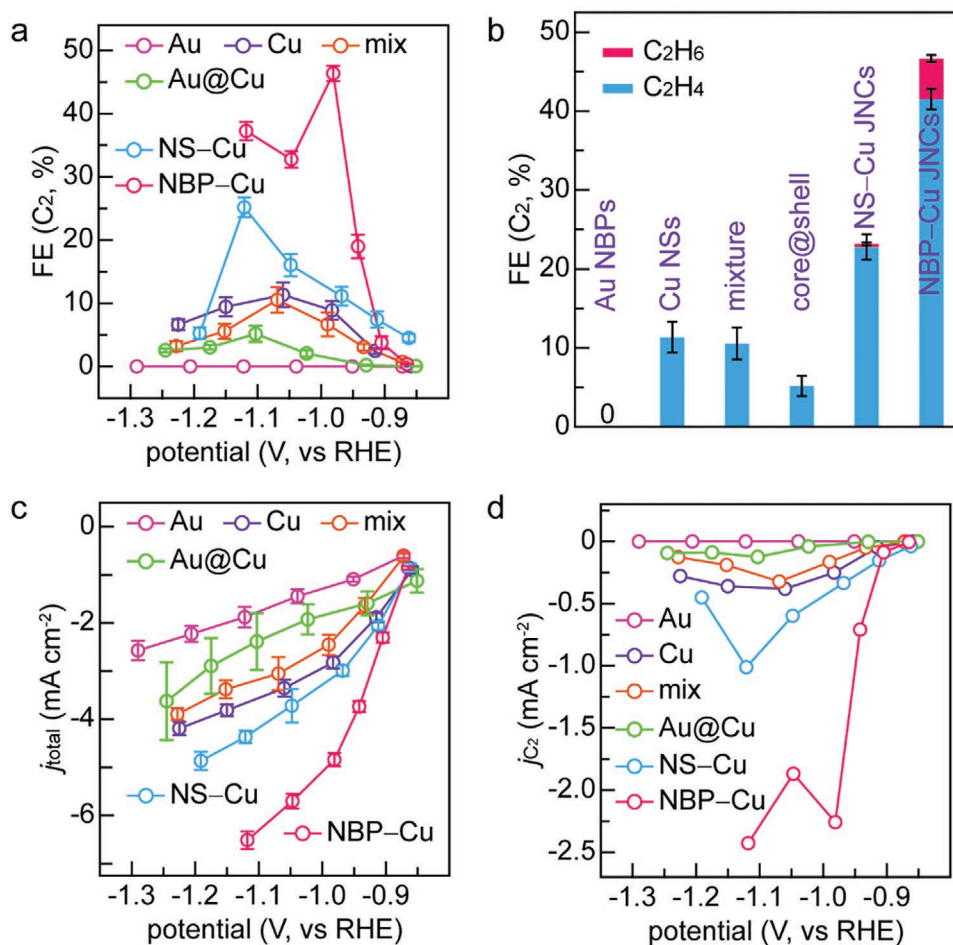
Figure 4. Comparison of the electrochemical CO_2 reduction performances. a) FEs of C_2 products obtained by using different catalysts. b) Comparison of optimal C_2 FE value obtained by using different catalysts. c) Total current density and d) C_2 product partial current density of different catalysts.
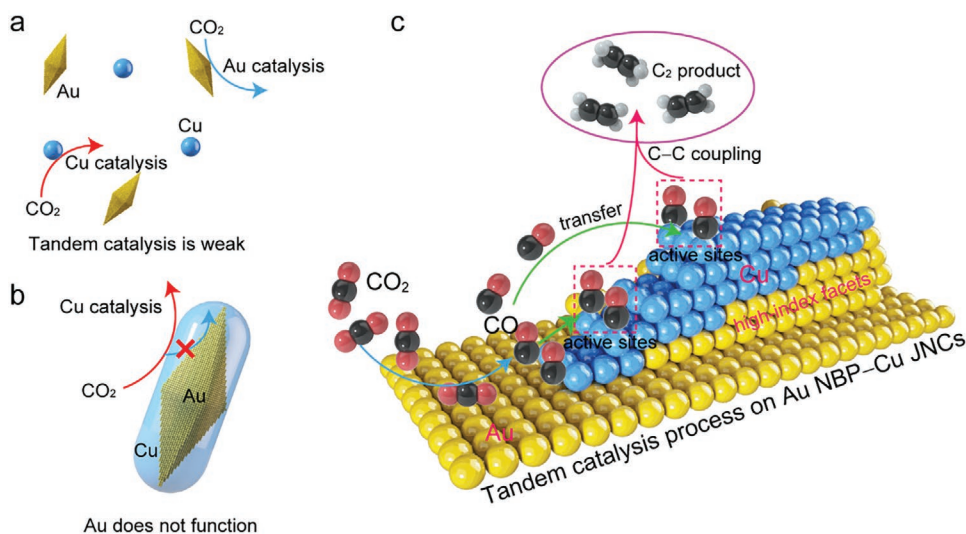

Figure 5. Proposed mechanism of the C_2 production on a) the mixture of the Au NBP and the Cu NS, b) the Au@Cu core@shell nanostructure, and c) the Au NBP–Cu JNC catalysts, respectively.

ADVANCED
SCIENCE NEWS
www.advancedsciencenews.com

ADVANCED
FUNCTIONAL
MATERIALS
www.afm-journal.de

(Figure 5b). In this scenario, catalysis can only take place on the surface of the Cu shell, and the Au core is actually not functional toward tandem electrocatalysis. In contrast, the spatially separated hybrid nanostructure and the intimate contact of two domains in the Au–Cu JNCs enable the occurrence of tandem catalysis process, which facilitates the generation of C_2 production (Figure 5c). In the first step of the tandem catalysis process, the catalytic activity for CO_2 reduction to CO depends on the energetic stabilization of COOH* intermediate by the active sites on Au nanocrystals.[34] Excellent CO_2 adsorption and activation capability of Au nanocrystals facilitate the conversion of CO_2 to CO. As shown in Figure S1, Supporting Information, Au NBPs are encapsulated with 10 high-index {116} facets. These high-index facets with abundant atomic steps can serve as the active sites for CO_2 adsorption and hydrogenation to generate COOH* intermediate. The Gibbs free energy required to form the COOH* intermediate on the high-index facets of Au NBPs is significantly lower than that on the low-index facets of Au NSs.[68] As a result, Au NBPs exhibit higher CO production activity (Figure 3a) than Au NSs (Figure S18, Supporting Information). In the second step, the atomic steps on Au NBPs can maximize the interfacial coupling with the supported Cu domains and optimize the binding of key intermediates in the C_2 pathway, boosting the generation of C_2 products.[7,69] Therefore, the Au NBP–Cu hybrid nanostructures can become superior electrocatalysts for the tandem catalysis process. Scattered atoms or clusters can work as active species for CO_2RR as well. Figures 1c and 2g indicate the possible presence of some scattered Cu atoms or clusters on Au nanocrystals, which are formed in the nucleation and growth steps. Previous researches demonstrated that small Cu nanoparticles (<5 nm) or Cu clusters may promote the reduction of water at the expense of the CO_2RR.[5,70] On the other hand, single-atom Cu catalyst favors the conversion of CO_2 to C_1 product,[71,72] while the C_2 product is hardly generated due to the lack of sufficient neighboring Cu atom ensembles that are critical for C—C coupling.[42] Thus, these possible scattered Cu atoms or clusters on Au nanocrystals make an almost negligible contribution to the C_2 product generation. In addition, the high C_2 product selectivity of the Au NBP–Cu JNC catalyst may be attributed to the suppression of hydrogen evolution. Up to now, several mechanisms have been proposed to explain the suppression of hydrogen evolution, including strain effect,[73] CO poisoning,[74] and electronic effect.[75] Strain-induced formation of surface alloy can improve the multicarbon product selectivity.[73] However, the strain effect has a negligible effect on the C_2 product selectivity because it is absent from the alloyed interfaces in the Au–Cu JNC structures (Figure 1d 3) and the Au atoms can hardly migrate to the whole surface of Cu domains for the alloying process. The worse performance of the core@shell nanostructures suggests that the strain effect does not play an important role in CO_2RR. In addition, the suppression of hydrogen evolution can be achieved by CO poisoning when the surface of Cu catalysts is covered by the adsorbed CO intermediates.[74] If CO poisoning occurs, the generation of CO will be depressed. Conversely, the relatively high CO FE values (Figure 3) of the Au–Cu JNC catalysts suggest that the CO poisoning is unlikely the underlying effect. A possible mechanism for the suppression of hydrogen evolution is the electronic effect.[75] The change of electronic structure

of Cu nanodomains after the growth on Au nanocrystals will modify the binding strength of intermediates according to the d-band model, which depresses the hydrogen evolution but promotes the CO and C_2 product generation.[75] Specifically, Au has a higher electron affinity (2.309 eV) than Cu (1.228 eV), facilitating the electron transfer from Cu to Au in this hybrid nanostructure[76] and resulting in a more positive binding energy of the Cu nanodomain than the bulk Cu counterparts (Figure S5b, Supporting Information). Electron-depleted Cu can increase the CO adsorption energy and consequently improve the CO dimerization yield, boosting the generation of C_2 products.[77] Above all, the synergistic effect of Au and Cu endows the Au NBP–Cu JNCs with high activity and good selectivity toward C_2 production.

3. Conclusions

In summary, a facile and general wet-chemistry method is developed for the synthesis of spatially separated Au NBP–Cu hybrid nanostructures on the basis of a large lattice mismatch between them. The concentrations of CTAB and HDA play crucial roles in the overgrowth of Cu nanodomains on the Au NBPs and determine the morphology of the Au–Cu nanostructures. The proposed synthesis method can be simply extended to other Au nanocrystals from 0D to 2D, enabling the production of diverse asymmetric Au–Cu nanostructures. In addition, the spatial-separation design of the Au–Cu heterostructure possesses distinct advantages over the Cu NSs in the activity and selectivity of C_2 production. The optimal FE value and maximum partial current density of the Au NBP–Cu JNCs are 4.1-fold and 6.4-fold compared with those of Cu counterparts. This can be ascribed to the tandem catalysis process promoted by the hybrid nanostructure and the high-index facets on the Au NBPs. This research provides an alternative strategy for the synthesis of spatially separated hybrid nanoblocks for efficient electrochemical reactions, and it opens a new avenue for pursuing high-efficiency catalysis through the manipulation of reaction pathways in CO_2RR.

4. Experimental Section

Chemicals: HDA (98%), copper(II) chloride ($CuCl_2$, 99.999%), ʟ-ascorbic acid (AA) (≥99%), sodium borohydride ($NaBH_4$, 99%), silver nitrate ($AgNO_3$, ≥99.0%), sodium citrate tribasic dihydrate (TSC, ≥99%), copper(II) fluoride (CuF_2, 98%), copper(II) bromide ($CuBr_2$, 99%), copper(I) iodide (CuI, 98%), copper(II) acetate monohydrate ($Cu(AC)_2$, ≥98%), dodecylamine (DDA, 98%), potassium bicarbonate ($KHCO_3$, 99.7%), potassium chloride (KCl, 99.0–100.5%), and Nafion 117 solution (≈5%) were purchased from Sigma-Aldrich. Tetrachloroauric(III) acid trihydrate ($HAuCl_4$ $3H_2O$), hydrochloric acid (HCl, ≈36.0–38.0 w%), ammonia solution (NH_3 H_2O, ≈25.0–28.0 wt%), hydrogen peroxide aqueous solution (H_2O_2, ≥30.0 wt%), sodium hydroxide (NaOH, ≥96.0%), and isopropanol (≥99.7%) were obtained from Sinopharm Chemical Reagent. Hexadecyltrimethylammonium chloride (CTAC, 97%), and potassium iodide (KI ≥99.0%) were obtained from Aladdin Reagent. CTAB (>98%) was purchased from Alfa Aesar. Octadecylamine (ODA, 90%) was obtained from Macklin. Carbon dioxide (CO_2, 99.999%), nitrogen (N_2, 99.999%), hydrogen (H_2, 99.999%), argon (Ar, 99.999%), and helium (He, 99.999%) were

used as received. Deionized water with a resistivity of 18.2 MΩ cm was used in all experiments.

Growth of the Au NBPs: The starting Au NBPs were prepared using a seed-mediated growth method in combination with a depletion force-induced purification process.[54,55] Specifically, the seed solution was made by injecting a freshly prepared, ice-cold $NaBH_4$ solution (10 mM, 125 μL) into an aqueous solution containing $HAuCl_4$ (10 mM, 125 μL), TSC (10 mM, 250 μL), and deionized water (9.625 mL) under vigorous stirring. The resultant seed solution was kept at room temperature for at least 2 h prior to use. The growth solution was prepared by the sequential addition of $HAuCl_4$ (10 mM, 2 mL), $AgNO_3$ (10 mM, 400 μL), HCl (1 M, 800 μL), and AA (0.1 M, 320 μL) into CTAB aqueous solution (0.1 M, 40 mL). The seed solution (200 μL) was then injected into the growth solution, followed by gentle inversion mixing for 10 s. The resultant solution was kept undisturbed overnight at room temperature. The obtained Au NBPs were further purified using a depletion force-induced purification process.[55]

Growth of the Au NBP–Cu Janus Nanostructures: Typically, the obtained Au NBP solution (5 mL) was centrifuged at 7500 rpm for 10 min, followed by washing with deionized water (5 mL) to remove the excess surfactant. The precipitate was redispersed in a CTAB solution (0.5 mM, 0.5 mL) to get a final CTAB concentration of 100 μM. For the overgrowth of Cu nanodomains on the Au NBPs, HDA (12 mg) was added in boiling water (8.575 mL) in a 25-mL three-necked round-bottom flask and refluxed in an oil bath at 100 °C under magnetic stirring. After the complete dissolution of HDA, $CuCl_2$ solution (0.1 M, 100 μL) was added and the mixture was kept stirring for more than 10 min to form the Cu(II)–HDA complexes. To initiate the overgrowth, the Au NBP solution (optical density at the longitudinal dipole plasmon wavelength = 15, 500 μL) was added, followed by the injection of AA solution (0.2 M, 825 μL). The total volume of the solution was adjusted to 10 mL by adding deionized water and the final concentrations of CTAB and HDA were 100 μM and 5 mM, respectively. The resultant solution was further refluxed at 100 °C for 1 h to produce the Au NBP–Cu JNCs, followed by cooling down to room temperature naturally.

Growth of the Other Au Nanocrystals and Au–Cu Nanostructures: The synthesis details were described in the Supporting Information.

Electrochemical Measurements: The working electrodes were prepared by drop-casting the catalyst (26 μg) onto a glassy carbon plate in an area of 1 cm^2 (1 cm × 0.5 cm × 2). Before the electrochemical tests, the as-prepared electrodes were stored in a vacuum oven to evaporate the solvent and to prevent the oxidation of catalysts.

The electrochemical measurements were conducted in a customized gastight two-compartment cell, that was composed of an anodic chamber and a cathodic chamber, separated by a Nafion 117 membrane. Each chamber was loaded with CO_2-saturated 0.1 M $KHCO_3$ aqueous solution (20 mL, pH = 6.8) as the electrolyte. A potentiostat (CHI 660E) equipped with a typical three-electrode system was employed for the CO_2RR experiments. The counter and reference electrode were a graphite rod and an Ag/AgCl (filled with saturated KCl solution) electrode, respectively. All potentials were recorded with the Ag/AgCl electrode and converted to the RHE scale according to E (vs RHE) = E (vs Ag/AgCl) + 0.197 V + 0.0591 × pH. The potentials (vs RHE) were further manually corrected to compensate for 85% Ohmic loss.[17,46] In order to calculate the FE, quantitative 5 Coulombs of charges were allowed to pass through the catalyst using chronoamperometry. Prior to each test, the working electrode was activated by passing through 2 Coulombs of charges.

Product Analysis: All gaseous products were quantitatively detected by an off-line gas chromatograph (GC, Agilent Technologies 7890B). The gas sample (2 mL) was taken using a syringe (2.5 mL, PTFE, Luer Lock valve, Agilent Technologies) from the headspace of the electrolytic cell and injected into the GC. Either He (99.999%) or N_2 (99.999%) was employed as the carrier gas. When He was used as the carrier gas, the gas sample was split into two aliquots for detection. One aliquot was routed through an HP-PLOT Al_2O_3/KCl capillary column and then quantitatively analyzed all major hydrocarbons using a flame ionization detector (FID), while the other was passed through a packed MoleSieve

5A column and CO was detected with a thermal conductivity detector (TCD). H_2 was detected using the TCD by passing through a packed MoleSieve 5A column with N_2 as the carrier gas. The liquid products (1 mL) were measured using either GC (Agilent Technologies 7890B) or an ion chromatograph (Thermo Fisher Scientific Aquion). Formate was detected using the ion chromatograph, while the other major liquid products were analyzed using the FID of GC by passing through a DB-WAX capillary column with N_2 as the carrier gas.

Characterization: TEM imaging was obtained by an HT7700 electron microscope operated at 100 kV. HRTEM, HAADF-STEM imaging, and elemental mapping were obtained by an FEI Tecnai F20 microscopy equipped with an Oxford energy-dispersive X-ray analysis system. The aberration-corrected HRTEM imaging was performed on a Titan Themis G3 ETEM (Thermo Scientific Company) at 300 kV. The extinction spectra were obtained by a Hitachi U-3900 ultraviolet/visible/NIR spectrophotometer. XRD patterns were obtained by a Smart Lab Se diffractometer equipped with Cu Kα radiation. XPS spectra were obtained by a Thermo Scientific ESCALAB 250Xi spectrometer. Inductively coupled plasma optical emission spectra (ICP-OES) were obtained by a PerkinElmer Optima 7300 DV system.

Supporting Information

Supporting Information is available from the Wiley Online Library or from the author.

Conflict of Interest

The authors declare no conflict of interest.

Data Availability Statement

Research data are not shared.

[1] P. D. Luna, C. Hahn, D. Higgins, S. A. Jaffer, T. F. Jaramillo, E. H. Sargent, *Science* **2019**, *364*, eaav3506.

[2] S. Nitopi, E. Bertheussen, S. B. Scott, X. Y. Liu, A. K. Engstfeld, S. Horch, B. Seger, I. E. L. Stephens, K. Chan, C. Hahn, J. K. Nørskov, T. F. Jaramillo, I. Chorkendorff, *Chem. Rev.* **2019**, *119*, 7610.

**ADVANCED
SCIENCE NEWS**

www.advancedsciencenews.com

**ADVANCED
FUNCTIONAL
MATERIALS**

www.afm-journal.de

[3] C.-T. Dinh, T. Burdyny, M. G. Kibria, A. Seifitokaldani, C. M. Gabardo, F. P. García de Arquer, A. Kiani, J. P. Edwards, P. D. Luna, O. S. Bushuyev, C. Q. Zou, R. Quintero-Bermudez, Y. J. Pang, D. Sinton, E. H. Sargent, *Science* **2018**, *360*, 783.

[4] D. Wakerley, S. Lamaison, F. Ozanam, N. Menguy, D. Mercier, P. Marcus, M. Fontecave, V. Mougel, *Nat. Mater.* **2019**, *18*, 1222.

[5] R. Reske, H. Mistry, F. Behafarid, B. R. Cuenya, P. Strasser, *J. Am. Chem. Soc.* **2014**, *136*, 6978.

[6] S. Popović, M. Smiljanić, P. Jovanovič, J. Vavra, R. Buonsanti, N. Hodnik, *Angew. Chem., Int. Ed.* **2020**, *59*, 14736.

[7] A. Vasileff, C. C. Xu, Y. Jiao, Y. Zheng, S.-Z. Qiao, *Chem* **2018**, *4*, 1809.

[8] D. F. Gao, R. M. Arán-Ais, H. S. Jeon, B. R. Cuenya, *Nat. Catal.* **2019**, *2*, 198.

[9] Y. Zheng, A. Vasileff, X. L. Zhou, Y. Jiao, M. Jaroniec, S.-Z. Qiao, *J. Am. Chem. Soc.* **2019**, *141*, 7646.

[10] L. Zhang, Z.-J. Zhao, J. L. Gong, *Angew. Chem., Int. Ed.* **2017**, *56*, 11326.

[11] Y. F. Li, F. Cui, M. B. Ross, D. Kim, Y. C. Sun, P. D. Yang, *Nano Lett.* **2017**, *17*, 1312.

[12] A. Loiudice, P. Lobaccaro, E. A. Kamali, T. Thao, B. H. Huang, J. W. Ager, R. Buonsanti, *Angew. Chem., Int. Ed.* **2016**, *55*, 5789.

[13] P. Grosse, D. F. Gao, F. Scholten, I. Sinev, H. Mistry, B. R. Cuenya, *Angew. Chem., Int. Ed.* **2018**, *57*, 6192.

[14] B. X. Zhang, J. L. Zhang, M. L. Hua, Q. Wan, Z. Z. Su, X. N. Tan, L. F. Liu, F. Y. Zhang, G. Chen, D. X. Tan, X. Y. Cheng, B. X. Han, L. R. Zheng, G. Mo, *J. Am. Chem. Soc.* **2020**, *142*, 13606.

[15] N.-T. Suen, Z.-R. Kong, C.-S. Hsu, H.-C. Chen, C.-W. Tung, Y.-R. Lu, C.-L. Dong, C.-C. Shen, J.-C. Chung, H. M. Chen, *ACS Catal.* **2019**, *9*, 5217.

[16] P. D. Luna, R. Quintero-Bermudez, C.-T. Dinh, M. B. Ross, O. S. Bushuyev, P. Todorović, T. Regier, S. O. Kelley, P. D. Yang, E. H. Sargent, *Nat. Catal.* **2018**, *1*, 103.

[17] W. Zhang, C. Q. Huang, Q. Xiao, L. Yu, L. Shuai, P. F. An, J. Zhang, M. Qiu, Z. F. Ren, Y. Yu, *J. Am. Chem. Soc.* **2020**, *142*, 11417.

[18] D. Ren, Y. L. Deng, A. D. Handoko, C. S. Chen, S. Malkhandi, B. S. Yeo, *ACS Catal.* **2015**, *5*, 2814.

[19] Q. Lei, H. Zhu, K. P. Song, N. N. Wei, L. M. Liu, D. L. Zhang, J. Yin, X. L. Dong, K. X. Yao, N. Wang, X. H. Li, B. Davaasuren, J. J. Wang, Y. Han, *J. Am. Chem. Soc.* **2020**, *142*, 4213.

[20] P.-P. Yang, X.-L. Zhang, F.-Y. Gao, Y.-R. Zheng, Z.-Z. Niu, X. X. Yu, R. Liu, Z.-Z. Wu, S. Qin, L.-P. Chi, Y. Duan, T. Ma, X.-S. Zheng, J.-F. Zhu, H.-J. Wang, M.-R. Gao, S.-H. Yu, *J. Am. Chem. Soc.* **2020**, *142*, 6400.

[21] C. Hahn, T. Hatsukade, Y.-G. Kim, A. Vailionis, J. H. Baricuatro, D. C. Higgins, S. A. Nitopi, M. P. Soriaga, T. F. Jaramillo, *Proc. Natl. Acad. Sci. U. S. A.* **2017**, *114*, 5918.

[22] Z. N. Wang, G. Yang, Z. R. Zhang, M. S. Jin, Y. D. Yin, *ACS Nano* **2016**, *10*, 4559.

[23] F. W. Li, A. Thevenon, A. Rosas-Hernández, Z. Y. Wang, Y. L. Li, C. M. Gabardo, A. Ozden, C. T. Dinh, J. Li, Y. H. Wang, J. P. Edwards, Y. Xu, C. McCallum, L. Z. Tao, Z.-Q. Liang, M. C. Luo, X. Wang, H. H. Li, C. P. O'Brien, C.-S. Tan, D.-H. Nam, R. Quintero-Bermudez, T.-T. Zhuang, Y. G. C. Li, Z. J. Han, R. D. Britt, D. Sinton, T. Agapie, J. C. Peters, E. H. Sargent, *Nature* **2020**, *577*, 509.

[24] Z. Weng, X. Zhang, Y. S. Wu, S. J. Huo, J. B. Jiang, W. Liu, G. J. He, Y. Y. Liang, H. L. Wang, *Angew. Chem., Int. Ed.* **2017**, *56*, 13135.

[25] Y. Chen, Z. X. Fan, J. Wang, C. Y. Ling, W. X. Niu, Z. Q. Huang, G. G. Liu, B. Chen, Z. C. Lai, X. Z. Liu, B. Li, Y. Zong, L. Gu, J. L. Wang, X. Wang, H. Zhang, *J. Am. Chem. Soc.* **2020**, *142*, 12760.

[26] D. Kim, C. L. Xie, N. Becknell, Y. Yu, M. Karamad, K. Chan, E. J. Crumlin, J. K. Nørskov, P. D. Yang, *J. Am. Chem. Soc.* **2017**, *139*, 8329.

[27] J. J. Fu, W. L. Zhu, Y. Chen, Z. Y. Yin, Y. Y. Li, J. Liu, H. Y. Zhang, J.-J. Zhu, S. H. Sun, *Angew. Chem., Int. Ed.* **2019**, *58*, 14100.

[28] Y. J. Han, Z. T. Wang, X. T. Han, W. S. Fang, Y. S. Zhou, K. Lei, B. You, H. S. Park, B. Y. Xia, *ACS Sustainable Chem. Eng.* **2021**, *9*, 2609.

[29] H. L. Jia, A. X. Du, H. Zhang, J. H. Yang, R. B. Jiang, J. F. Wang, C.-Y. Zhang, *J. Am. Chem. Soc.* **2019**, *141*, 5083.

[30] S. Mubeen, J. Lee, N. Singh, S. Krämer, G. D. Stucky, M. Moskovits, *Nat. Nanotechnol.* **2013**, *8*, 247.

[31] M. W. Knight, H. Sobhani, P. Nordlander, N. J. Halas, *Science* **2011**, *332*, 702.

[32] E. C. Dreaden, A. M. Alkilany, X. H. Huang, C. J. Murphy, M. A. El-Sayed, *Chem. Soc. Rev.* **2012**, *41*, 2740.

[33] R. Zhu, J. Li, L. S. Lin, J. B. Song, H. H. Yang, *Adv. Funct. Mater.* **2020**, *31*, 2005709.

[34] W. L. Zhu, R. Michalsky, Ö. Metin, H. F. Lv, S. J. Guo, C. J. Wright, X. L. Sun, A. A. Peterson, S. H. Sun, *J. Am. Chem. Soc.* **2013**, *135*, 16833.

[35] R. G. Mariano, K. McKelvey, H. S. White, M. W. Kanan, *Science* **2017**, *358*, 1187.

[36] S. Zhao, R. X. Jin, R. C. Jin, *ACS Energy Lett.* **2018**, *3*, 452.

[37] J. H. Lee, S. Kattel, Z. H. Xie, B. M. Tackett, J. J. Wang, C.-J. Liu, J. G. G. Chen, *Adv. Funct. Mater.* **2018**, *28*, 1804762.

[38] Y. Y. Birdja, E. Pérez-Gallent, M. C. Figueiredo, A. J. Göttle, F. Calle-Vallejo, M. T. M. Koper, *Nat. Energy* **2019**, *4*, 732.

[39] C. G. Morales-Guio, E. R. Cave, S. A. Nitopi, J. T. Feaster, L. Wang, K. P. Kuhl, A. Jackson, N. C. Johnson, D. N. Abram, T. Hatsukade, C. Hahn, T. F. Jaramillo, *Nat. Catal.* **2018**, *1*, 764.

[40] X. L. Wang, J. F. de Araújo, W. Ju, A. Bagger, H. Schmies, S. Kühl, J. Rossmeisl, P. Strasser, *Nat. Nanotechnol.* **2019**, *14*, 1063.

[41] X. Zhao, L. J. Du, B. You, Y. J. Sun, *Catal. Sci. Technol.* **2020**, *10*, 2711.

[42] S. C. Ma, M. Sadakiyo, M. Heima, R. Luo, R. T. Haasch, J. I. Gold, M. Yamauchi, P. J. A. Kenis, *J. Am. Chem. Soc.* **2017**, *139*, 47.

[43] X. C. Pang, C. S. Wan, M. Y. Wang, Z. Q. Lin, *Angew. Chem., Int. Ed.* **2014**, *53*, 5524.

[44] Z. Q. Huang, J. L. Gong, Z. H. Nie, *Acc. Chem. Res.* **2019**, *52*, 1125.

[45] Y. G. Sun, *Natl. Sci. Rev.* **2015**, *2*, 329.

[46] J. F. Huang, M. Mensi, E. Oveisi, V. Mantella, R. Buonsanti, *J. Am. Chem. Soc.* **2019**, *141*, 2490.

[47] S. G. Kwon, G. Krylova, P. J. Phillips, R. F. Klie, S. Chattopadhyay, T. Shibata, E. E. Bunel, Y. Z. Liu, V. B. Prakapenka, B. Lee, E. V. Shevchenko, *Nat. Mater.* **2015**, *14*, 215.

[48] J. C. Wang, X. L. Wu, W. Ma, C. L. Xu, *Adv. Funct. Mater.* **2020**, *30*, 2000670.

[49] J. Liu, J. T. Zhang, *Chem. Rev.* **2020**, *120*, 2123.

[50] T. H. Chow, N. N. Li, X. P. Bai, X. L. Zhuo, L. Shao, J. F. Wang, *Acc. Chem. Res.* **2019**, *52*, 2136.

[51] M. Z. Liu, P. Guyot-Sionnest, *J. Phys. Chem. B* **2005**, *109*, 22192.

[52] X. S. Kou, S. Z. Zhang, C.-K. Tsung, M. H. Yeung, Q. H. Shi, G. D. Stucky, L. D. Sun, J. F. Wang, C. H. Yan, *J. Phys. Chem. B* **2006**, *110*, 16377.

[53] Z. N. Wang, Z. Z. Chen, H. Zhang, Z. R. Zhang, H. J. Wu, M. S. Jin, C. Wu, D. R. Yang, Y. D. Yin, *ACS Nano* **2015**, *9*, 3307.

[54] X. S. Kou, W. H. Ni, C.-K. Tsung, K. Chan, H.-Q. Lin, G. D. Stucky, J. F. Wang, *Small* **2007**, *3*, 2103.

[55] Q. Li, X. L. Zhuo, S. Li, Q. F. Ruan, Q.-H. Xu, J. F. Wang, *Adv. Opt. Mater.* **2015**, *3*, 801.

[56] C.-F. Hsia, M. Madasu, M. H. Huang, *Chem. Mater.* **2016**, *28*, 3073.

[57] F. Qin, T. Zhao, R. B. Jiang, N. N. Jiang, Q. F. Ruan, J. F. Wang, L.-D. Sun, C.-H. Yan, H.-Q. Lin, *Adv. Opt. Mater.* **2016**, *4*, 76.

[58] M. S. Jin, G. N. He, H. Zhang, J. Zeng, Z. X. Xie, Y. N. Xia, *Angew. Chem., Int. Ed.* **2011**, *50*, 10560.

[59] M. S. Jin, H. Zhang, J. G. Wang, X. L. Zhong, N. Lu, Z. Y. Li, Z. X. Xie, M. J. Kim, Y. N. Xia, *ACS Nano* **2012**, *6*, 2566.

**ADVANCED
SCIENCE NEWS**

www.advancedsciencenews.com

**ADVANCED
FUNCTIONAL
MATERIALS**

www.afm-journal.de

[60] R. He, Y.-C. Wang, X. Y. Wang, Z. T. Wang, G. Liu, W. Zhou, L. P. Wen, Q. X. Li, X. P. Wang, X. Y. Chen, J. Zeng, J. G. Hou, *Nat. Commun.* **2014**, *5*, 4327.

[61] V. Kumar, V. Patil, A. Apte, N. Harale, P. Patil, S. Kulkarni, *Langmuir* **2015**, *31*, 13247.

[62] M. B. Ross, P. D. Luna, Y. F. Li, C.-T. Dinh, D. Kim, P. D. Yang, E. H. Sargent, *Nat. Catal.* **2019**, *2*, 648.

[63] P. Godbold, G. Johnson, A. D. Obi, R. Brown, S. Hwang, R. J. Gilliard Jr., S. Zhang, *J. Am. Chem. Soc.* **2021**, *143*, 2644.

[64] C. Y. Zhu, Z. B. Zhang, L. X. Zhong, C.-S. Hsu, X. Z. Xu, Y. Z. Li, S. W. Zhao, S. H. Chen, J. Y. Yu, S. L. Chen, M. Wu, P. Gao, S. Z. Li, H. M. Chen, K. H. Liu, L. M. Zhang, *Chem* **2021**, *7*, 406.

[65] E. L. Clark, J. Resasco, A. Landers, J. Lin, L.-T. Chung, A. Walton, C. Hahn, T. F. Jaramillo, A. T. Bell, *ACS Catal.* **2018**, *8*, 6560.

[66] P. Iyengar, J. F. Huang, G. L. De Dregorio, C. Gadiyar, R. Buonsanti, *Chem. Commun.* **2019**, *55*, 8796.

[67] K. D. Yang, W. R. Ko, J. H. Lee, S. J. Kim, H. Lee, M. H. Lee, K. T. Nam, *Angew. Chem., Int. Ed.* **2017**, *56*, 796.

[68] C. Xiao, B.-A. Lu, P. Xue, N. Tian, Z.-Y. Zhou, X. Lin, W.-F. Lin, S.-G. Sun, *Joule* **2020**, *4*, 2562.

[69] H.-E. Lee, K. D. Yang, S. M. Yoon, H.-Y. Ahn, Y. Y. Lee, H. Chang, D. H. Jeong, Y.-S. Lee, M. Y. Kim, K. T. Nam, *ACS Nano* **2015**, *9*, 8384.

[70] J. F. Huang, N. Hörmann, E. Oveisi, A. Loiudice, G. L. De Gregorio, O. Andreussi, N. Marzari, R. Buonsanti, *Nat. Commun.* **2018**, *9*, 3117.

[71] C. C. Xu, A. Vasileff, Y. Zheng, S.-Z. Qiao, *Adv. Mater. Interfaces* **2020**, *8*, 2001904.

[72] Y. M. Cai, J. J. Fu, Y. Zhou, Y.-C. Chang, Q. H. Min, J.-J. Zhu, Y. H. Lin, W. L. Zhu, *Nat. Commun.* **2021**, *12*, 586.

[73] E. L. Clark, C. Hahn, T. F. Jaramillo, A. T. Bell, *J. Am. Chem. Soc.* **2017**, *139*, 15848.

[74] Y.-J. Zhang, V. Sethuraman, R. Michalsky, A. A. Peterson, *ACS Catal.* **2014**, *4*, 3742.

[75] D. Kim, J. Resasco, Y. Yu, A. M. Asiri, P. D. Yang, *Nat. Commun.* **2014**, *5*, 4948.

[76] M. Tsuji, D. Yamaguchi, M. Matsunaga, M. J. Alam, *Cryst. Growth Des.* **2010**, *10*, 5129.

[77] Y. S. Zhou, F. L. Che, M. Liu, C. Q. Zou, Z. Q. Liang, P. D. Luna, H. F. Yuan, J. Li, Z. Q. Wang, H. P. Xie, H. M. Li, P. N. Chen, E. Bladt, R. Quintero-Bermudez, T.-K. Sham, S. Bals, J. Hofkens, D. Sinton, G. Chen, E. H. Sargent, *Nat. Chem.* **2018**, *10*, 974.